Opto-Electronic Advances

ISSN 2096-4579 CN 51-1781/TN

Spin-controlled generation of a complete polarization set with randomly-interleaved plasmonic metasurfaces

Sören im Sande, Yadong Deng, Sergey I. Bozhevolnyi and Fei Ding

Citation: im Sande S, Deng YD, Bozhevolnyi SI, et al. Spin-controlled generation of a complete polarization set with randomly-interleaved plasmonic metasurfaces. *Opto-Electron Adv* **7**, 240076(2024).

https://doi.org/10.29026/oea.2024.240076

Received: 3 April 2024; Accepted: 12 June 2024; Published online: 23 July 2024

Opto-Electronic Advances

Article

August 2024, Vol. 7, No. 8

DOI: 10.29026/oea.2024.240076

Spin-controlled generation of a complete polarization set with randomly-interleaved plasmonic metasurfaces

Sören im Sande, Yadong Deng, Sergey I. Bozhevolnyi and Fei Ding*

Optical metasurfaces, comprising subwavelength quasi-planar nanostructures, constitute a universal platform for manipulating the amplitude, phase, and polarization of light, thus paving a way for the next generation of highly integrated multifunctional optical devices. In this work, we introduce a reflective metasurface for the generation of a complete (angularly resolved) polarization set by randomly interleaving anisotropic plasmonic meta-atoms acting as nanoscale wave plates. In the proof-of-concept demonstration, we achieve multidirectional beam-steering into different polarization channels forming a complete set of polarization states, which can also be dynamically altered by switching the spin of incident light. The developed design concept represents a significant advancement in achieving flat polarization optics with advanced functionalities.

Keywords: plasmonic metasurface; randomly interleaved; multidirectional beam-steering; spin-controlled; all-polarization generation

im Sande S, Deng YD, Bozhevolnyi SI et al. Spin-controlled generation of a complete polarization set with randomly-interleaved plasmonic metasurfaces. *Opto-Electron Adv* **7**, 240076 (2024).

Introduction

Manipulation of light, comprising its amplitude, phase, and polarization, is crucial for advancements across a broad spectrum of technologies, ranging from optical communication, display technologies, to optical computing. Optical metasurfaces, acclaimed for their unique role in the miniaturization and multifunction trends, stand at the forefront of these innovations, offering compact device footprints at the micrometer scale while enabling subwavelength-level control over all degrees of freedom of light[1–12]. Among all applications, metasurface-empowered polarization optics[13] has been extensively investigated, allowing for the generation[14–24] and manipulation[25–33] of polarization, one intrinsic characteristic of optical waves, which is uncorrelated with the amplitude and phase. Specifically, the capacity to independently control the phase of two orthogonal polarizations facilitates the integration of waveplate functionalities into anisotropic metasurfaces, thereby enabling polarization-specific operations[14–20,34–36]. This advancement underscores the metasurface's potential to realize complex optical functionalities and implement them in compact, efficient designs. The development of polarization-coded multifunctional metasurfaces represents a leap in optical technologies allowing one to combine a broader spectrum of functionalities into a single metasurface[13,25–30,37–40]. The polarization-coded integration is achieved through innovative meta-atom designs and/or by clever interweaving

Centre for Nano Optics, University of Southern Denmark, Odense 5230, Denmark.
*Correspondence: F Ding, E-mail: feid@mci.sdu.dk
Received: 3 April 2024; Accepted: 12 June 2024; Published online: 23 July 2024

of distinct metasurfaces, each tailored for specific functions. These advancements herald a new era in photonics, where metasurfaces serve as versatile platforms for a multitude of optical applications, exemplifying the ongoing progress towards more integrated and dynamically controllable optical elements.

Despite noteworthy achievements, most metasurfaces demonstrated to date have been constrained to generating a limited set of polarization states distributed across a few channels. Approaches to generate a (close to) complete set of polarization channels in a controlled manner have rarely been reported, not to mention approaches enabling switchable polarization states in the different channels. Here, we introduce a reflective metasurface for the generation of a complete (angularly resolved) polarization set by randomly interleaving anisotropic plasmonic meta-atoms, acting as nanoscale wave plates with properly designed phase retardations. Our approach enables multidirectional beam-steering across all polarization channels with judiciously designed polarization states that can also be altered by switching the spin of incident light.

Results and discussion

Schematic of a proposed gold-silica-gold (Au-SiO_2-Au) plasmonic metasurface[41], which executes multidirectional beam-steering into a complete set of angularly-resolved polarization channels by randomly interleaving six distinct metasurface pixels (meta-pixels), is shown in Fig. 1(a). Notably, each meta-pixel is meticulously engineered to uniquely alter the polarization state of incident left- or right-handed circularly polarized (LCP or RCP) light, reflecting the polarization-altered light into the corresponding unique direction in the far-field. Once the spin of the incident CP light is reversed, the states of polarization change to their orthogonal counterparts. These meta-pixels are structured into square 8×8 arrays of meta-atoms acting as nanoscale wave plates, except for one that remains unstructured to serve as a mirror meta-pixel, reflecting co-polarized circular CP light (reduced 4×4 arrays are shown in Fig. 1(b)). Furthermore, the meta-atoms embody different designs depending on the emulated wave-plate functionality. The meta-pixel responsible for the transformation between LCP and RCP states incorporate brick-shaped meta-atoms, which act as

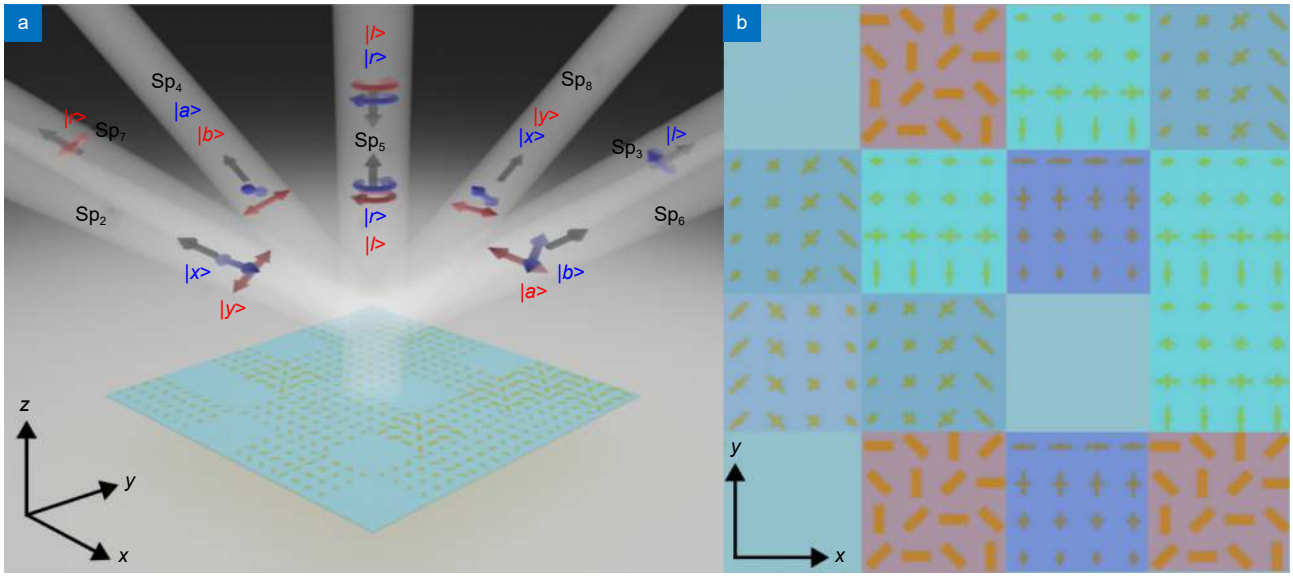

Fig. 1 | Conceptualization of the plasmonic metasurface for generating a complete polarization set. (**a**) Illustration of the Au-SiO_2-Au metasurface that reflects and additionally splits a CP incident beam into six spatially separated channels, each featuring a specific polarization state. The polarization states change to their orthogonal counterparts when the spin of the incident light is reversed. The RCP incidence generates spots Sp_2, Sp_3, Sp_4, Sp_5, Sp_6, and Sp_8, respectively, whereas LCP incidence produces spots Sp_2, Sp_4, Sp_5, Sp_6, Sp_7, and Sp_8, respectively. The absolute values of polar angles for deflected LP and CP spots are around 15.4° and 22.1°, respectively, at the design wavelength of 850 nm. (**b**) Top view of a metasurface segment that consists of six different kinds of interleaved meta-pixels with the mirror (empty spaces), HWP (bricks, marked in red), and QWP (crosses, marked in blue color) functionalities. The mirror and HWP meta-pixels produce co-polarized and cross-polarized circular polarization states, respectively, while the QWP meta-pixels, differentiated by four distinct orientations, generate four unique linear polarization states. |*x*>, |*y*>, |*a*>, and |*b*> represent horizontal, vertical, 45°, and −45° linear polarizations, respectively. For illustrative purposes, each meta-pixel is reduced to 4 × 4 meta-atoms. The change of spin due to reflection is not considered here.

half-wave plates (HWPs) to transform the incident CP light into the cross-polarized light[41–43]. Within a specific meta-pixel, the HWP meta-atoms are methodically rotated in increments of 45°, with each row being offset by one element (Fig. 1(b)), a design that generates a geometric phase gradient in both *x*- and *y*-directions for the reflected light, facilitating thereby the angular separation from the co-polarized reflection by the mirror meta-pixels. In contrast, the meta-pixels responsible for CP reflection into linearly polarized (LP) light comprise cross-shaped meta-atoms with different orientations, which serve as quarter-wave plates (QWPs) enabling the generation and routing of different LP beams[21]. In this case, linear phase gradients in either *x*- or *y*-direction are introduced for QWP meta-pixels by varying dimensions of meta-atoms in the vicinity of the gap surface plasmon (GSP) resonance, unlike geometric phase gradients by meta-atom rotations employed in HWP meta-pixels[13]. This difference in implementing the phase gradients is intimately related to differences in the underlying physics of HWP and QWP operations for CP light incidence: while the meta-atom rotation in the former influences only the phase of reflected cross-CP light, the meta-atom rotation in the latter would result in the polarization rotation of reflected LP light[13].

The dimensions of HWP and QWP meta-atoms were optimized through full-wave simulations with COMSOL Multiphysics (version 5.6), employing a parameter sweep across lateral dimensions within a unit cell defined by periodic boundary conditions in the *x*- and *y*-directions. Perfectly matched layers capped the simulation domain to minimize external interference. The thickness of the Au meta-atoms, the foundational Au mirror, and the SiO_2 spacer were predetermined based on the QWP meta-atoms design criteria, requiring the occurrence of the GSP resonance in the design parameter space that is instrumental in realizing the resonant phase gradient by varying meta-atom dimensions[21]. For the rotated HWP meta-atom (Fig. 2(a)), a geometric phase equivalent to twice the angle of rotation is introduced, while the reflection amplitude maintains a high level above 0.92 at the design wavelength of 850 nm, indicating negligible near-field coupling between adjacent elements. Remarkably, the HWP meta-atoms are predicted to demonstrate significant broadband reflectivity into +1 diffraction order when arranged into a supercell composed of 1 × 8 meta-atoms for creating a linear phase gradient along the *x*-direction (Fig. 2(b)). Moreover, the phase gradient depends on the spin of the incident light, where switching between RCP and LCP excitation inversely alters the diffraction order (Fig. S1). To establish the linear phase gradient necessary for spatially separating the generated LP beams, four distinct QWP meta-atoms are designed, each introducing a 90° resonance phase step relative to adjacent meta-atoms (Fig. 2(c)). Each element is then duplicated in the supercell to decrease the diffraction angle, slightly reducing the efficiency compared to a four-element supercell (Fig. S2). Although the QWP supercell exhibits lower reflectivity into +1 diffraction order compared to the HWP counterpart, the beam-steering performance at the design wavelength of 850 nm is expected to be rather good (Fig. 2(d)) given the necessity of having near-resonant meta-atoms to comply with the design criteria[21]. Unlike the HWP configuration, altering the incident spin does not impact the diffracted spatial direction (Fig. S1) due to the spin-insensitive nature of the resonant phase[13]. Instead, two orthogonal CP beams yield two distinct, yet orthogonal, linear polarizations. Specifically, LP beams with angles of linear polarization (AoLPs) equal to $\theta \pm 45°$ are accordingly created for RCP and LCP incident beams with near unity degrees of linear polarization (DoLPs) (Fig. S3). For instance, QWP meta-pixels comprising meta-atoms rotated at −45°, 0°, 45°, and 90° generate four distinct linear polarizations $|x\rangle$, $|a\rangle$, $|y\rangle$, and $|b\rangle$ ($|y\rangle$, $|b\rangle$, $|x\rangle$, and $|a\rangle$), respectively, under the RCP (LCP) excitation. To validate the polarization set generation, we used standard thin-film deposition, electron beam lithography (EBL), and lift-off processes to fabricate the sample with an area of 80 μm × 80 μm (see Experimental Section for details). As depicted in Fig. 3, the fabricated metasurface exhibits a commendable alignment with our theoretical design, where randomly interleaved meta-pixels are clearly seen under both the optical microscope and scanning electron microscope (SEM), albeit accompanied by certain limitations. For example, the diminutive crosses constituting the QWP meta-atoms display less distinct cross-shaped geometries (Fig. 3(d) to 3(g)), a deviation primarily attributed to the inherent constraints of our fabrication equipment. Specifically, during electron beam lithography (EBL), cross-shaped meta-atoms are decomposed into smaller polygons for exposure. These polygons vary in shape for each orientation, potentially leading to less defined corners at the cross's center and, consequently, exposure discrepancies.

After fabrication, we characterized the sample using a

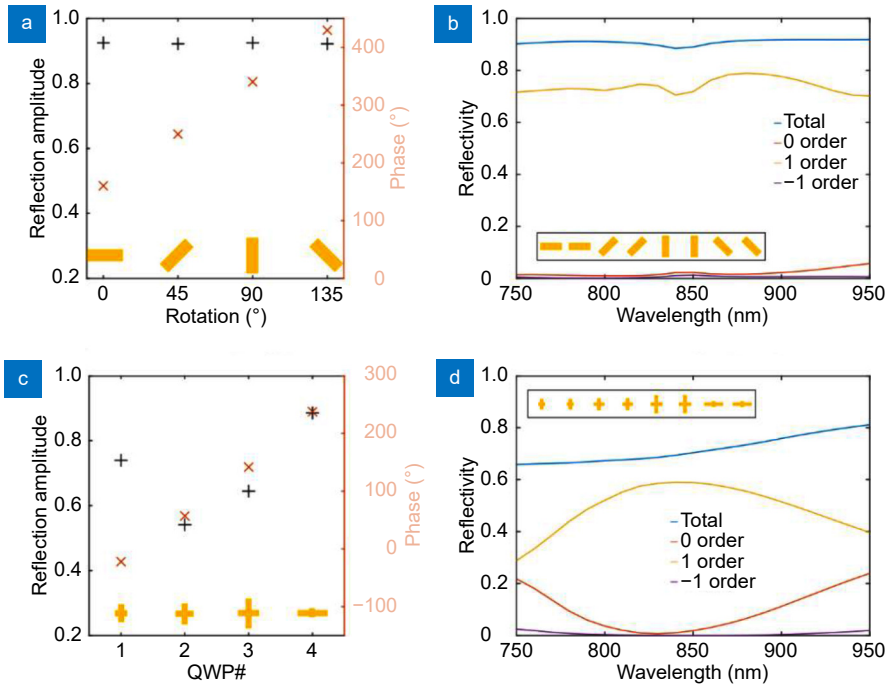

Fig. 2 | Performance of the meta-atoms under RCP incidence. (**a**) Simulated reflection amplitude and phase of the four HWP meta-atoms with different orientations at the design wavelength of 850 nm. (**b**) Simulated diffraction efficiencies of the HWP supercell, shown in the inset, as a function of wavelength. (**c**) Simulated reflection amplitude and phase of the four QWP meta-atoms at the design wavelength of 850 nm. (**d**) Simulated diffraction efficiencies of the QWP supercell, shown in the inset as a function of wavelength. The dimensions of all selected meta-atoms are shown in Table S1.

homemade optical setup (Fig. S4), where the polarization generation was validated not only at the target wavelength of 850 nm (Fig. 4) but also at additional wavelengths of 750 nm (Fig. S5) and 900 nm (Fig. S6). While some degree of noise is observable —likely a consequence of the complex interplay between multiple meta-pixels—the six distinct polarization channels remain discernibly isolated within the Fourier plane, superior to the simulated results with a reduced metasurface area (Fig. S7). For both RCP and LCP incidence, four diffracted beams (Sp_2, Sp_4, Sp_6, and Sp_8) with feature linear polarization states are produced by four corresponding QWP meta-pixels with *x*- or *y*-oriented linear phase gradients (Fig. 4(a) to 4(d)), whose intensities are distinctly altered by changing the transmission axis of the analyzer (Fig. 4(f), 4(h), 4(j), and 4(l)). Once the spin is varied, the generated linear polarization state switches to its orthogonal counterpart with high extinction ratios. The measured DoLPs surpass 85%, with the peak value reaching 98.8%. Correspondingly, the retrieved Stokes parameter S_1 or S_2 is larger (smaller) than 0.85 (−0.85) and the maximum (minimum) value approaches 0.97 (−0.97). The measured efficiencies (intensity ratio between the deflected light and the total reflected light) of the generated LP beams fall within the range of 2.5% to 5%, which are considerably low due to the substantial background noise (~28%) from the randomly interleaved configuration[31]. The observed variability in DoLPs and efficiencies can be traced back to nuances in the fabrication process. Apart from the linear polarization generation, the co- and cross-polarized CP beams are reflected by the mirror and HWP meta-pixels, respectively. For the RCP incident light, only spot Sp_3 with the cross-polarization state is visible since the spin-dependent phase gradient is along the positive diagonal direction. When the incident light switches to LCP, spot Sp_7 becomes pronounced while spot Sp_3 disappears, with efficiency exceeding ~3%. The measured degrees of circular polarization (DoCPs, corresponding to Stokes parameter S_3) or ellipticities of the CP beams reflected from the HWP meta-pixels exhibit a range between 0.79 and 0.82 for incidence at the wavelength of 850 nm, and between 0.67 and 0.93 for incidence at the wavelengths of 750 nm, 850 nm, and 900 nm. This variation is largely explicable by the initial imperfections in CP light incidence (Fig. 4(e)), indicated by the polar plot of the specular reflections from the mirror meta-pixels (Fig. 4(i)).

Finally, we investigate the working performance of our metasurface under the excitation of $|y>$ state at the target wavelength of 850 nm (Fig. 5), as well as at 750 nm (Fig.

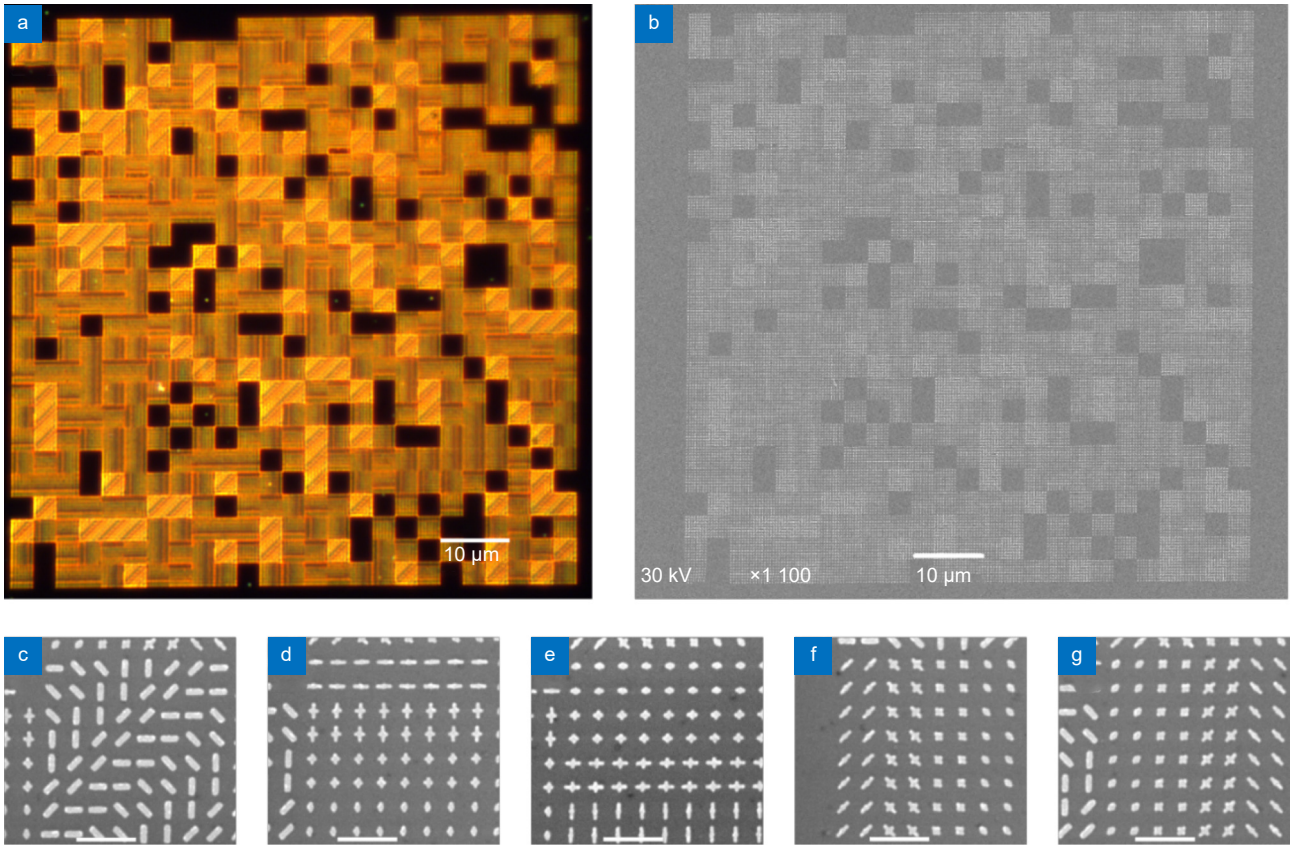

Fig. 3 | Optical microscope (**a**) and SEM (**b**–**g**) images of the fabricated metasurface. The scale bars in (c–g) are 1 μm. The meta-pixels shown in (c–g) generate respectively the reflection of LCP (RCP) at 45° (135°), |*a*> (|*b*>) at 180°, |*b*> (|*a*>) at 0°, |*x*> (|*y*>) at 90° and |*y*> (|*x*>) at 270° under the RCP (LCP) incidence.

S8) and 900 nm (Fig. S9). Different from the CP incidence, the |*y*> excitation can only generate limited polarization states, although seven diffraction spots are formed. The QWP meta-pixels, wherein one of the cross arms is aligned with the incident polarization, enable *y*-polarized beam generation with high DoLPs of approximately 98% and the Stokes parameter S_1 of around –0.92 (Fig. 5(h) and 5(j)). Conversely, QWP meta-pixels oriented at ±45° relative to the incident polarization failed to generate the intended CP light (Stokes parameter S_3 of only ±0.6), a phenomenon attributable to fabrication discrepancies. Moreover, the HWP meta-pixels effectively function as beam splitters to generate two orthogonal CP light components (Fig. 5(g) and 5(k)). However, this configuration results in diminished DoCPs of the reflected polarizations, registering between 0.70 and 0.78 at a wavelength of 850 nm.

Conclusion

In conclusion, our study introduces a general plasmonic metasurface capable of generating a complete and angularly resolved polarization set through the randomly interleaved arrangement of anisotropic plasmonic meta-atoms that allow simultaneous and independent control over the polarization and phase. This intricate design allows for the dynamic manipulation of polarization states by merely altering the spin of the incident light, showcasing a remarkable ability for multidirectional beam-steering into six typical polarization channels. The successful demonstration of this concept not only marks a significant leap forward in the field of polarization optics but also paves the way for developing compact, efficient, and highly functional optical devices. By leveraging the unique properties of these nanoscale wave plates, our work opens new avenues for exploring advanced optical applications, from imaging and sensing to communications and beyond. The potential implications of this technology are vast, offering a promising future for the realization of sophisticated optical systems that can be dynamically controlled, thereby enhancing the versatility and performance of optical components across a myriad of disciplines.

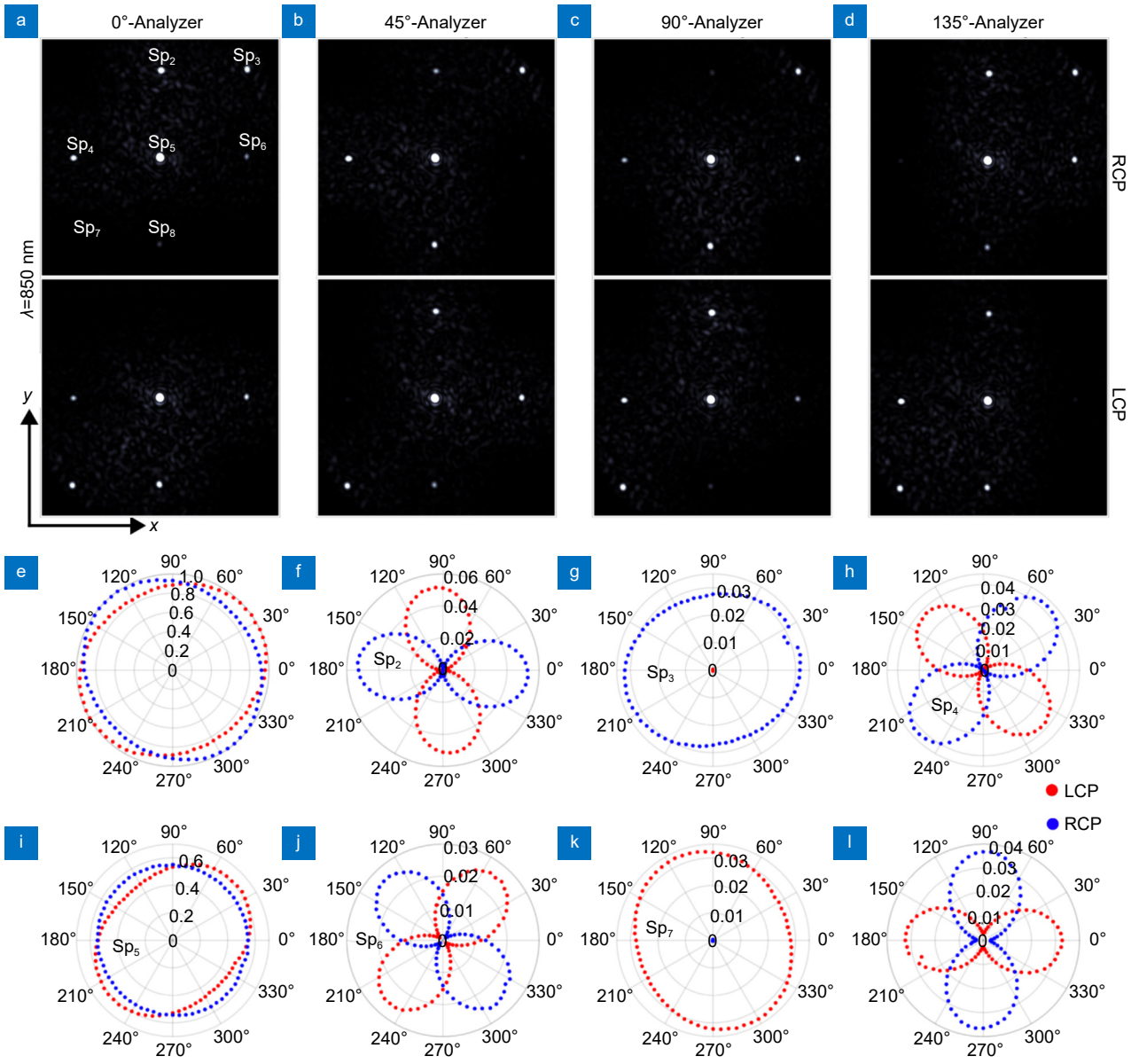

Fig. 4 | Experimental demonstration of spin-controlled polarization set generation at the design wavelength of 850 nm. (**a**–**d**) Polarization-resolved intensity profiles. The feature spots are marked as Sp_2-Sp_8 for future analysis. (**e**) Polar plots of the RCP (blue) and LCP (red) incident beams. (**f**, **h**, **j**, and **l**) Polar plots of the diffracted LP beams (Sp_2, Sp_4, Sp_6, and Sp_8) from the QWP meta-pixels with cross arms oriented at −45° (f), 0° (h), 90° (j), and 45° (l), respectively. The AoLPs are rotated by 90° once the incident light is switched from RCP to LCP. (g, k) Polar plots of the diffracted CP beams (Sp_3 and Sp_7) from the HWP meta-pixels. Only the cross-polarized CP beam is visible, with its handedness altered by the spin of incident light. (**i**) Polar plot of reflected CP beams (Sp_5) with co-polarization states from the mirror meta-pixels.

Experimental Section

Fabrication

The fabrication includes thin-film deposition, EBL, and lift-off processes. The consecutive deposition of a 3 nm titanium (Ti) layer, a 100 nm Au layer, and a 2 nm Ti layer on a silicon substrate was done using thermal vapor deposition. Afterward, RF sputtering was utilized to deposit a SiO_2 spacer layer with a thickness of 100 nm. Then, an approximately 100 nm thick PMMA (2% in anisole, Micro Chem) layer was spin-coated as an electron beam resist, which was then baked at 180°C for 2 min. This resist was exposed to define the meta-atoms at an acceleration voltage of 30 kV. A solution of methyl isobutyl ketone (MIBK) and isopropyl alcohol (IPA) of MIBK: IPA = 1∶3 was used as a developer for 35 s and pure IPA as a stopper. After that, a 2 nm Ti layer and a 40 nm gold layer were deposited through thermal vapor

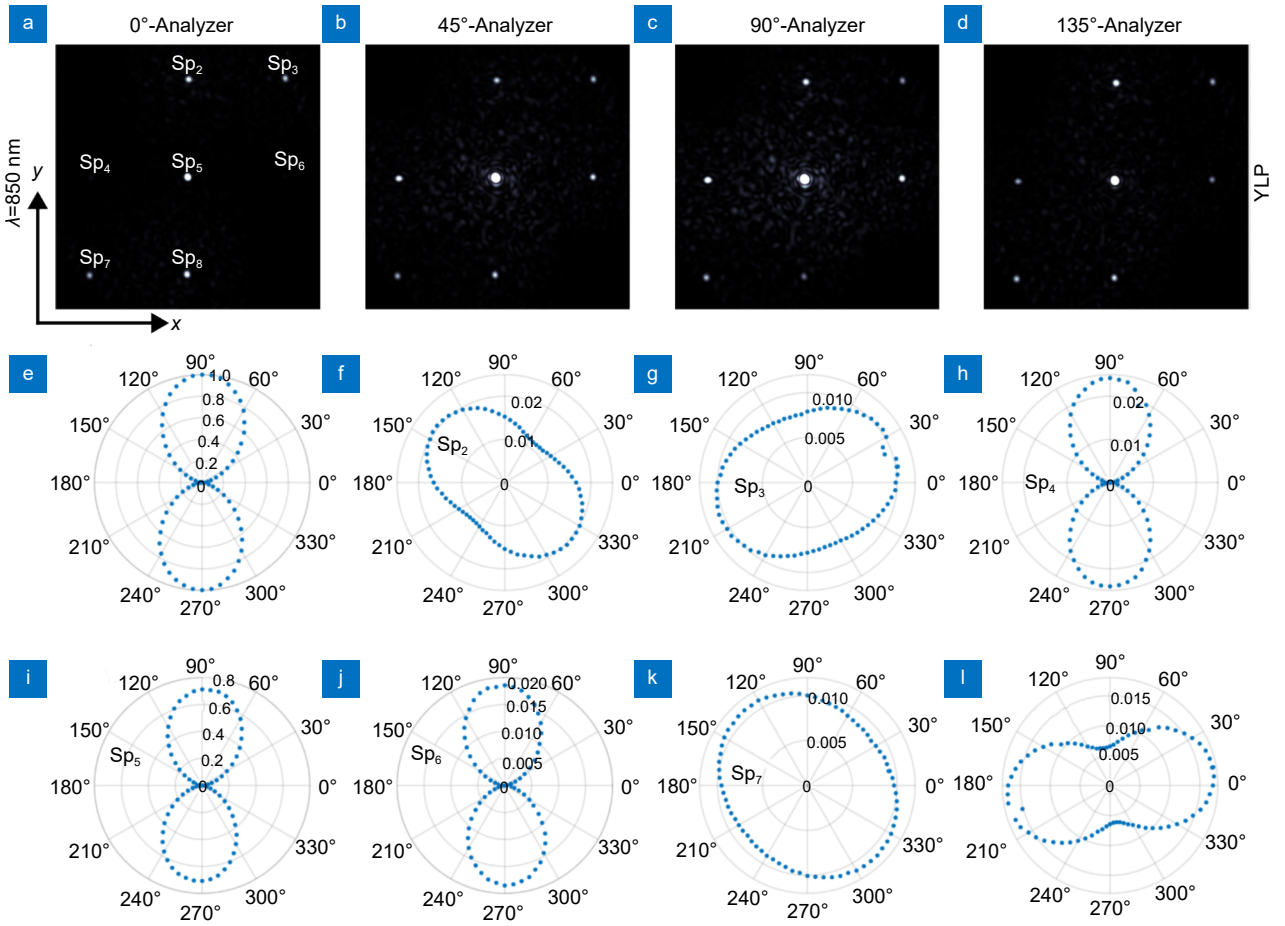

Fig. 5 | Operation performance of the metasurface for *y*-polarized incident light at the design wavelength of 850 nm. (**a**–**d**) Polarization-resolved intensity profiles. The feature spots are marked as Sp_2-Sp_8 for future analysis. (**e**) Polar plot of the *y*-polarized incident beam. (**f**, **l**) Polar plots of the diffracted elliptically polarized beams (Sp_2 and Sp_8) from the QWP meta-pixels with cross arms oriented at −45° (**f**) and 45° (**l**), respectively. (**g**, **k**) Polar plots of the diffracted CP beams (Sp_3 and Sp_7) from the HWP meta-pixels. Both LCP and RCP beams are visible, each receiving half of the power as the incoming light splits. (**h**, **j**) Polar plots of the diffracted *y*-polarized beams (Sp_4 and Sp_6) from the QWP meta-pixels with cross arms oriented at 0° (h) and 90° (j), respectively. (**i**) Polar plot of the reflected *y*-polarized beam (S_5) from the mirror meta-pixels.

deposition. The unexposed PMMA was finally lifted off in acetone and the fabrication result was evaluated through SEM.

Measurements

The measurements were conducted with a homebuilt optical setup (Fig. S4). The light from SuperK Extreme laser (NKT Photonics) passes through first an attenuator and then a combination of a linear polarizer and a quarter wave plate to create the CP light with controlled intensity. The CP light passes through two identical beam splitters before reaching the sample through an objective (Nikon E Plan 100× / 0.90 EPI). The two beam splitters are used to compensate for the actual phase retardance caused by one single beam splitter. Furthermore, a lens (Lens 1, Thorlabs LA1608-B-ML) in between the beam splitters, in combination with the objective, produces a plane wave incident on the sample. The reflected signal is collected by the same objective and then passes through a tube lens (Lens2, Thorlabs TTL200-S8) and an iris to select the region of interest in the fabricated sample. To filter out the different CP components, a linear polarizer and a quarter-wave plate have been added. Two more lenses (Lens3, Thorlabs AC254-125-B-ML and Fliplens4, Thorlabs LBF254-100-B) are used to switch between the direct and Fourier images captured by a CMOS camera (Thorlabs DCC1545M-GL). The direct image combined with a white light source is used to image the samples and position the laser spot, whereas Fourier images serve as the reconstructed Fourier images and image the holograms.

References

1. Kildishev AV, Boltasseva A, Shalaev VM. Planar photonics with metasurfaces. *Science* **339**, 1232009 (2013).
2. Yu NF, Capasso F. Flat optics with designer metasurfaces. *Nat Mater* **13**, 139–150 (2014).
3. Hsiao HH, Chu CH, Tsai DP. Fundamentals and applications of metasurfaces. *Small Methods* **1**, 1600064 (2017).
4. Sun SL, He Q, Hao JM et al. Electromagnetic metasurfaces: physics and applications. *Adv Opt Photonics* **11**, 380–479 (2019).
5. Ding F, Pors A, Bozhevolnyi SI. Gradient metasurfaces: a review of fundamentals and applications. *Rep Prog Phys* **81**, 026401 (2018).
6. Capasso F. The future and promise of flat optics: a personal perspective. *Nanophotonics* **7**, 953–957 (2018).
7. Chen HT, Taylor AJ, Yu NF. A review of metasurfaces: physics and applications. *Rep Prog Phys* **79**, 076401 (2016).
8. Kuznetsov AI, Brongersma ML, Yao J et al. Roadmap for optical metasurfaces. *ACS Photonics* **11**, 816–865 (2024).
9. Liu ZY, Wang DY, Gao H et al. Metasurface-enabled augmented reality display: a review. *Adv Photonics* **5**, 034001 (2023).
10. Shi YZ, Song QH, Toftul I et al. Optical manipulation with metamaterial structures. *Appl Phys Rev* **9**, 031303 (2022).
11. Liu Y, Shi YY, Wang ZJ et al. On-chip integrated metasystem with inverse-design wavelength demultiplexing for augmented reality. *ACS Photonics* **10**, 1268–1274 (2023).
12. Zhang C, Chen L, Lin ZL et al. Tantalum pentoxide: a new material platform for high-performance dielectric metasurface optics in the ultraviolet and visible region. *Light Sci Appl* **13**, 23 (2024).
13. Ding F, Tang SW, Bozhevolnyi SI. Recent advances in polarization‐encoded optical metasurfaces. *Adv Photonics Res* **2**, 2000173 (2021).
14. Hao JM, Yuan Y, Ran LX et al. Manipulating electromagnetic wave polarizations by anisotropic metamaterials. *Phys Rev Lett* **99**, 063908 (2007).
15. Pors A, Bozhevolnyi SI. Efficient and broadband quarter-wave plates by gap-plasmon resonators. *Opt Express* **21**, 2942–2952 (2013).
16. Jiang SC, Xiong X, Hu YS et al. Controlling the polarization state of light with a dispersion-free metastructure. *Phys Rev X* **4**, 021026 (2014).
17. Yang YM, Wang WY, Moitra P et al. Dielectric meta-reflectarray for broadband linear polarization conversion and optical vortex generation. *Nano Lett* **14**, 1394–1399 (2014).
18. Wu PC, Tsai WY, Chen WT et al. Versatile polarization generation with an aluminum plasmonic metasurface. *Nano Lett* **17**, 445–452 (2017).
19. Ding F, Chang BD, Wei QS et al. Versatile polarization generation and manipulation using dielectric metasurfaces. *Laser Photonics Rev* **14**, 2000116 (2020).
20. Wang DY, Liu FF, Liu T et al. Efficient generation of complex vectorial optical fields with metasurfaces. *Light Sci Appl* **10**, 67 (2021).
21. Deng YD, Wu C, Meng C et al. Functional metasurface quarter-wave plates for simultaneous polarization conversion and beam steering. *ACS Nano* **15**, 18532–18540 (2021).
22. Meng C, Thrane PCV, Ding F et al. Full-range birefringence control with piezoelectric MEMS-based metasurfaces. *Nat Commun* **13**, 2071 (2022).
23. Wu C, Kumar S, Kan YH et al. Room-temperature on-chip orbital angular momentum single-photon sources. *Sci Adv* **8**, eabk3075 (2022).
24. Pors A, Nielsen MG, Bozhevolnyi SI. Broadband plasmonic half-wave plates in reflection. *Opt Lett* **38**, 513–515 (2013).
25. Arbabi A, Horie Y, Bagheri M et al. Dielectric metasurfaces for complete control of phase and polarization with subwavelength spatial resolution and high transmission. *Nat Nanotechnol* **10**, 937–943 (2015).
26. Balthasar Mueller JP, Rubin NA, Devlin RC et al. Metasurface polarization optics: independent phase control of arbitrary orthogonal states of polarization. *Phys Rev Lett* **118**, 113901 (2017).
27. Zhang C, Divitt S, Fan QB et al. Low-loss metasurface optics down to the deep ultraviolet region. *Light Sci Appl* **9**, 55 (2020).
28. Meng C, Tang SW, Ding F et al. Optical gap-surface plasmon metasurfaces for spin-controlled surface plasmon excitation and anomalous beam steering. *ACS Photonics* **7**, 1849–1856 (2020).
29. Li ZL, Chen C, Guan ZQ et al. Three-channel metasurfaces for simultaneous meta-holography and meta-nanoprinting: a single-cell design approach. *Laser Photonics Rev* **14**, 2000032 (2020).
30. Huo PC, Zhang C, Zhu WQ et al. Photonic spin-multiplexing metasurface for switchable spiral phase contrast imaging. *Nano Lett* **20**, 2791–2798 (2020).
31. Sande SI, Bozhevolnyi SI, Ding F. Broadband spin-multiplexed single-celled metasurface holograms: a comprehensive comparison between different strategies. *Nanophotonics* **12**, 1363–1371 (2023).
32. Song MW, Feng L, Huo PC et al. Versatile full-colour nanopainting enabled by a pixelated plasmonic metasurface. *Nat Nanotechnol* **18**, 71–78 (2023).
33. Intaravanne Y, Wang RX, Ahmed H et al. Color-selective three-dimensional polarization structures. *Light Sci Appl* **11**, 302 (2022).
34. Ming Y, Intaravanne Y, Ahmed H et al. Creating composite vortex beams with a single geometric metasurface. *Adv Mater* **34**, 2109714 (2022).
35. Zhang YX, Pu MB, Jin JJ et al. Crosstalk-free achromatic full Stokes imaging polarimetry metasurface enabled by polarization-dependent phase optimization. *Opto-Electron Adv* **5**, 220058 (2022).
36. Huang YJ, Xiao TX, Chen S et al. All-optical controlled-NOT logic gate achieving directional asymmetric transmission based on metasurface doublet. *Opto-Electron Adv* **6**, 220073 (2023).
37. Liu WW, Li ZC, Ansari MA et al. Design strategies and applications of dimensional optical field manipulation based on metasurfaces. *Adv Mater* **35**, 2208884 (2023).
38. Zhang F, Guo YH, Pu MB et al. Meta-optics empowered vector visual cryptography for high security and rapid decryption. *Nat Commun* **14**, 1946 (2023).
39. Huang YJ, Xie X, Pu MB et al. Dual-functional metasurface toward giant linear and circular dichroism. *Adv Opt Mater* **8**, 1902061 (2020).
40. Bao HL, Zhang F, Pu MB et al. Field-driven inverse design of high-performance polarization-multiplexed meta-devices. *Laser Photonics Rev* 2301158 (2024).
41. Ding F, Yang YQ, Deshpande RA et al. A review of gap-surface plasmon metasurfaces: fundamentals and applications.

Nanophotonics **7**, 1129–1156 (2018).

42. Zheng GX, Mühlenbernd H, Kenney M et al. Metasurface holograms reaching 80% efficiency. *Nat Nanotechnol* **10**, 308–312 (2015).
43. Qiu YC, Tang SW, Cai T et al. Fundamentals and applications of spin-decoupled pancharatnam–berry metasurfaces. *Front Optoelectron* **14**, 134–147 (2021).

Acknowledgements

This work was funded by the Danmarks Frie Forskningsfond (1134-00010B) and Villum Fonden (Award in Technical and Natural Sciences 2019 and Grant No. 37372). Y. Deng would like to acknowledge the support from the China Scholarship Council (Grant No. 202108330079).

Author contributions

F. Ding proposed the original idea and initiated the project. S. im Sande and Y. D. Deng designed the metaatoms. S. im Sande fabricated the samples and conducted the measurements. S. I. Bozhevolnyi and F. Ding supervised the project. S. im Sande and F. Ding wrote the first draft of the manuscript. All authors commented on the manuscript.

Competing interests

The authors declare no competing financial interests.

Supplementary information

Supplementary information for this paper is available at https://doi.org/10.29026/oea.2024.240076

Scan for Article PDF